CROSS-CONTROLNET: TRAINING-FREE FUSION OF MULTIPLE CONDITIONS FOR TEXT-TO-IMAGE GENERATION

Anonymous authors
Paper under double-blind review

ABSTRACT

Text-to-image diffusion models achieve impressive performance, but reconciling multiple spatial conditions usually requires costly retraining or labor intensive weight tuning. We introduce **Cross-ControlNet**, a training-free framework for text-to-image generation with multiple conditions. It exploits two observations: intermediate features from different ControlNet branches are spatially aligned, and their condition strength can be measured by spatial and channel level variance. Cross-ControlNet contains three modules: **PixFusion**, which fuses features pixelwise under the guidance of standard deviation maps smoothed by a Gaussian to suppress early-stage noise; **ChannelFusion**, which applies per channel hybrid fusion via a consistency ratio gate, reducing *threshold degradation* in high dimensions; and **KV-Injection**, which injects foreground- and background-specific key/value pairs under text-derived attention masks to disentangle conflicting cues and enforce each condition faithfully. Extensive experiments demonstrate that Cross-ControlNet consistently improves controllable generation under both conflicting and complementary conditions, and further generalizes to the DiT-based FLUX model without additional training.

1 INTRODUCTION

In recent years, text-to-image (T2I) diffusion models (Podell et al., 2023; Balaji et al., 2022; Saharia et al., 2022; Chen et al., 2024b; Xue et al., 2023) have demonstrated unprecedented proficiency in image generation. These models can produce a wide variety of high-quality images from concise text prompts, effectively bridging the gap between human language and visual content. This achievement has not only captured the imagination of researchers and practitioners, but has also found broad applications in digital art, graphic design, and illustration generation (Wang et al., 2025a; Chen et al., 2023; Wang et al., 2025c; Chen et al., 2024a). However, the inherent ambiguity and abstractness of language make it extremely challenging for T2I models to achieve fine-grained control over the semantic layout of images (Li et al., 2023b). To address this issue, ControlNet (Zhang et al., 2023) and T2I-Adapter (Mou et al., 2024) incorporate spatial conditions (e.g., edges) into pretrained T2I models by introducing additional control networks, making controllable generation under a single modality no longer out of reach. Both approaches have achieved high-fidelity image synthesis while maintaining strong coherence with the structural conditions. Yet, when extended to multiple conditions, the inherent imbalance among different modalities means that each generation requires careful manual tuning of weighting coefficients—a significant burden (Nair et al., 2024). Consequently, synthesizing images that satisfy multiple conditions remains challenging (Wang et al., 2024).

A straightforward strategy is to train on large-scale paired data spanning diverse conditional modalities in order to learn how to balance multiple controls (Sun et al., 2024; Qin et al., 2023; Zhao et al., 2023a). Although effective, such approaches incur huge training costs and, when new modalities are introduced, almost always require partial or full retraining, which limits their flexibility. Moreover, when processing multiple control conditions, these methods tend to neglect weaker control signals. Recognizing that powerful pretrained controllable models (e.g., ControlNet) are already publicly available, some recent works (Nair et al., 2024; Wang et al., 2025b) such as MaxFusion avoid retraining and instead design fusion strategies to combine multiple ControlNet branches. However, the fusion strategy of MaxFusion is easily disrupted by the noise inherent in the denoising process, especially during the early sampling steps when latent variables exhibit high uncertainty (Karras et al., 2022; Cao et al., 2023). In addition, because it does not explicitly model the relationships between spatial conditions, it often struggles to generate harmonious images when the control signals are complex or partially conflicting.

In this paper we present **Cross-ControlNet**, a training-free framework for multimodal conditional generation (Fig. 2). Our design is driven by two key observations: (i) intermediate features from different ControlNet branches are spatially aligned; and (ii) the strength of these conditions can be quantified via spatial and channel-wise variance (Section 3.1). Leveraging these insights, we introduce three tightly coupled components that progressively refine feature fusion and enhance conditional consistency.

We first introduce **PixFusion**, which performs pixel-level fusion under the guidance of Gaussian-smoothed spatial standard deviation (Section 3.2). By enhancing informative features and suppressing early-stage noise, PixFusion offers an effective, noise-resilient approach for multi-condition feature fusion.1 However, pixel-level decisions alone suffer from the well-known phenomenon where, as feature dimensionality increases, cosine similarities cluster near zero, causing a fixed threshold to lose discriminative power rapidly. To alleviate this, we propose **ChannelFusion**, which operates along the channel dimension and, for each channel, adaptively applies either *hard selection* or *soft fusion* according to the channel-wise consistency ratio R_c (Section 3.2). This mechanism effectively counteracts the loss of discriminative power in high-dimensional settings and complements PixFusion's pixel-level fusion. Although PixFusion and ChannelFusion enhance the fusion of spatial conditions, conflicting multimodal signals can blur the roles of foreground and background, undermining precise conditional control. To stabilize generation in such cases, we introduce **KV-Injection**, which transfers key–value pairs across ControlNet branches under text-derived attention masks (Section 3.3); this mechanism temporarily decouples foreground and background cues so that each condition can be enforced more faithfully, thereby improving visual quality and conditional consistency.

Together, these three modules enable Cross-ControlNet to handle both conflicting conditions—where control signals impose contradictory spatial cues—and complementary conditions—where different controls reinforce the same scene structure. Our method preserves text–image alignment while accurately following the supplied spatial controls. On a newly curated 2,000-image multi-condition benchmark, Cross-ControlNet improves mIoU by 5.4% and lowers MSE over the strongest training-free baseline under conflicting conditions while maintaining text alignment, and further boosts SSIM under complementary conditions. We further demonstrate its adaptability by producing qualitative results on the DiT-based FLUX model, showing that Cross-ControlNet transfers effectively beyond UNet backbones (see Appendix A.5).

2 RELATED WORK

Controllable generation. Text-to-image diffusion models often lack fine-grained spatial control, motivating the use of auxiliary conditions in addition to text prompts. Early works introduce specific signals—such as layouts/boxes (Zheng et al., 2023; Xie et al., 2023), semantic segmentation maps (Avrahami et al., 2023), sketches (Bashkirova et al., 2023), and human pose keypoints (Ju et al., 2023)—to anchor generation and enable interactive or artistic design (Bar-Tal et al., 2023).More general frameworks (Mo et al., 2024; Zhang et al., 2023; Mou et al., 2024; Tan et al., 2024) emerged; among them, ControlNet duplicates the UNet encoder to encode single-modal conditions (e.g., pose, segmentation) into latent features that are injected into the diffusion UNet. To handle multiple spatial constraints, recent methods (Hu et al., 2023; Qin et al., 2023; Sun et al., 2024; Nair et al., 2024; Sun et al., 2025) either train unified multimodal models or combine several pretrained ControlNets. However, these approaches (Hu et al., 2023; Sun et al., 2024; Nair et al., 2024) often fail to produce harmonious and natural images when control signals interact in complex or conflicting ways.

Training-free image editing. Cross-attention manipulation enables text-driven edits without fine-tuning—for example, Prompt-to-Prompt and Plug-and-Play (Hertz et al., 2022; Tumanyan et al., 2023) preserve structural consistency by modifying queries or keys but give limited control over value (V) features and thus struggle with large non-rigid transformations. Subsequent works inject key–value pairs to maintain consistency across editing tasks that involve multiple images (Cao et al., 2023; Tewel et al., 2024; Alaluf et al., 2024; Zhu et al., 2025; Li, 2024; Chung et al., 2024).

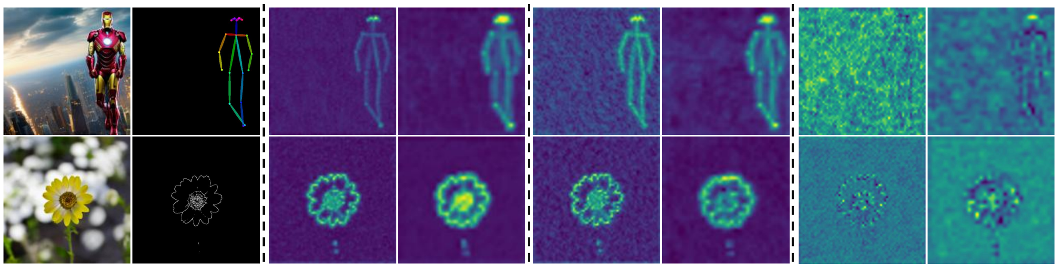

Figure 1: Visualization of intermediate-feature statistics for different ControlNet modalities. Columns 1–2: original image and its corresponding control map. Columns 3–4: spatial-level variance maps. Columns 5–6: feature maps from the single channel with relatively high variance across channels. Columns 7–8: feature maps from the single channel with relatively low variance across channels.

Inspired by these ideas, we inject key–value pairs across multiple ControlNet branches, allowing foreground–background decoupling and improving conditional consistency in both complementary and conflicting settings while retaining the flexibility of text-to-image generation.

3 METHODS

3.1 GUIDING OBSERVATIONS

Before presenting the details of our method, we first introduce two key observations that motivate our design.

Observation 1: Alignment of cross-modality features. Features produced by different ControlNet branches at identical spatial locations in Stable Diffusion (SD) (Rombach et al., 2022) exhibit natural spatial alignment. ControlNet encodes each conditional input into feature maps and injects them into SD's intermediate layers through element-wise summation. Because the outputs from different ControlNets enter SD at the same spatial positions, their features share a common reference frame and can be compared directly across modalities without any additional spatial calibration.

Observation 2: Quantifiable condition strength. The strength of each control condition can be directly or indirectly quantified via *spatial-level variance maps* and *channel-wise variance vectors*. As illustrated in Fig. 1, spatial variance maps of diverse control signals highlight regions where the condition exerts stronger influence, while channels with larger variance values indicate a more pronounced response to that condition. Together, these measures provide a reliable estimate of each condition's relative strength across both spatial regions and feature channels, enabling informed feature selection during fusion.

Taken together, these observations provide empirical grounding for our design: cross-modal feature fusion can be systematically guided by simple, quantifiable measures of condition strength. Building on this, our approach performs targeted feature fusion across modalities, enabling more faithful and consistent image generation under multimodal conditions.

3.2 ROBUST FEATURE FUSION

Let us begin with a simple setting: fusing two independent modalities. Consider two ControlNet models M_1 and M_2 that process different types of input (e.g., edge detection and semantic segmentation) and produce intermediate features f_1 and f_2, respectively. A naive strategy is to average these features, but equal weighting often fails when each modality dominates a different spatial region (for example, left vs. right halves of the image). In such cases, uniform averaging dilutes crucial information, motivating the need for adaptive fusion.

PixFusion. An ideal fusion method should assign different priorities to different spatial locations (j, k) according to the local conditional intensity, which can be measured by spatial-level variance maps $\sigma_i^2 \in \mathbb{R}^{H\times W}$. To make the variance maps from different modalities comparable, we introduce

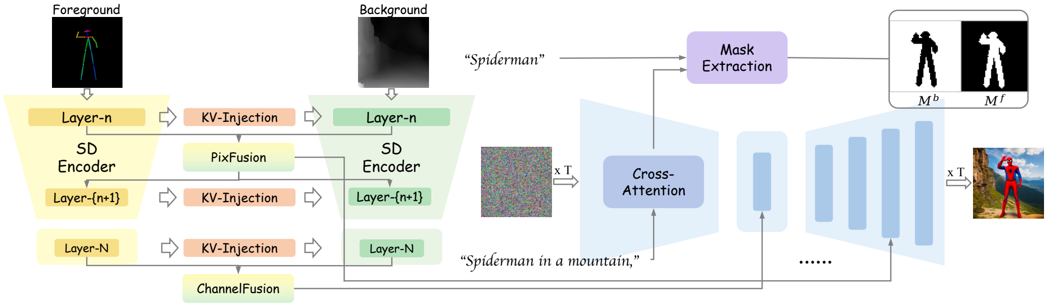

(a) Overall Pipeline of Cross-ControlNet

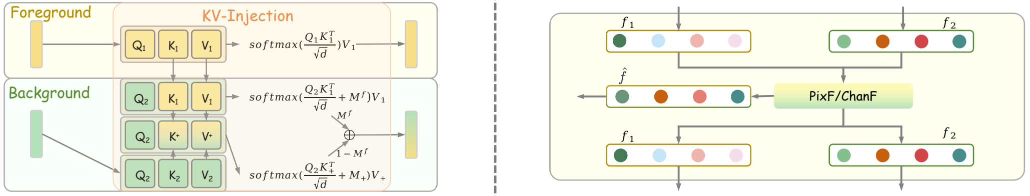

(b) KV-Injection (c) PixFusion or ChannelFusion

Figure 2: Cross-ControlNet Overview. (a) Intermediate features from different ControlNet modalities are first fused through either PixFusion or ChannelFusion, and the fused features are then injected into the main denoising backbone. In parallel, the key–value pairs from the self-attention layers of the foreground ControlNet are injected into the corresponding layers of the background ControlNet. (b) KV-Injection mechanism. Foreground and background key–value pairs are selectively merged within the self-attention layers to enforce cross-modal consistency. (c) Intermediate features are subsequently fused via PixFusion or ChannelFusion.

a relative standard-deviation metric that normalizes the variance at each spatial location:

$$\hat{\sigma}_i^{(j,k)} = \frac{\sigma_i^{(j,k)}}{\sum_{(p,q)\in\Omega} \sigma_i^{(p,q)}}. \tag{1}$$

Directly comparing these normalized maps, however, can be unreliable because the standard deviation maps themselves are contaminated by noise. Recall that the diffusion process generates images by iterative denoising: at early sampling stages the latent space still contains strong high-frequency noise. Pixel-wise fusion at this stage would therefore make the fused features highly susceptible to distortion.

To mitigate this, we apply Gaussian kernel smoothing, which yields the following fusion rule:

$$\hat{f}^{(j,k)} = f_{i^\star}^{(j,k)}, \quad i^\star = \arg\max_i \big[\mathcal{G}_{\kappa_1} * \hat{\sigma}_i\big]_{(j,k)}, \tag{2}$$

where $\mathcal{G}_{\kappa_1}$ is a fixed Gaussian kernel and $[\mathcal{G}_{\kappa_1} * \hat{\sigma}_i]_{(j,k)}$ represents the value at location (j,k) after smoothing, i.e., an average over its neighborhood rather than a single pixel.

Nevertheless, blindly choosing the channel with the largest standard deviation is not always desirable. When multimodal conditions overlap—meaning different modalities describe the same object—it is preferable to integrate information from both. To this end we compute the correlation at each location (j,k) and, whenever features are strongly correlated, we adopt mean fusion:

$$\hat{f}^{(j,k)} = \frac{f_1^{(j,k)} + f_2^{(j,k)}}{2}, \quad \text{if } \rho^{(j,k)} > \delta_1, \tag{3}$$

where δ_1 is a predefined threshold and $\rho^{(j,k)}$ denotes the correlation between the centered features $f_1^{(j,k)}$ and $f_2^{(j,k)}$. Because these correlations can also be distorted by noise, we again apply Gaussian smoothing:

$$\rho^{(j,k)} = \frac{f_1'^{(j,k)} \cdot f_2'^{(j,k)}}{\|f_1'^{(j,k)}\| \, \|f_2'^{(j,k)}\|}, \qquad f_i' = (f_i - \bar{f}_i) *_{\text{group}=\mathcal{C}} \mathcal{G}_{\kappa_2}, \qquad \bar{f}_i^{(j,k)} = \frac{1}{\mathcal{C}} \sum_{c=1}^{\mathcal{C}} f_i^{(j,k)}(c), \tag{4}$$

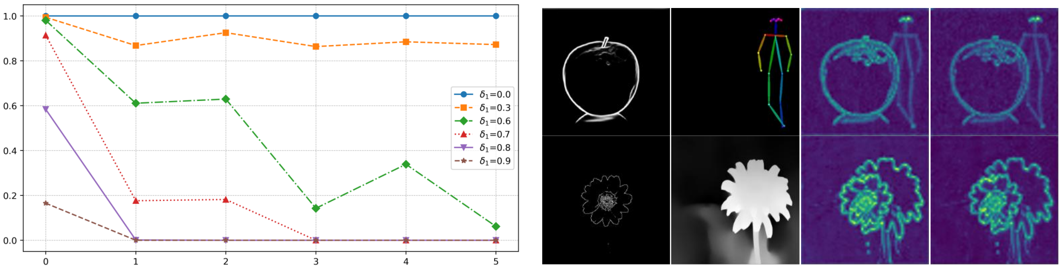

(a) (b)

Figure 3: (a) Threshold degradation curve for different δ_1 values. The horizontal axis indicates the depth of the feature layer, and the vertical axis indicates the proportion reaching the fusion threshold. (b) Variance maps of the fused intermediate features. Column 3: after PixFusion; Column 4: after ChannelFusion.

where $\mathcal{G}_{\kappa_2}$ is a fixed Gaussian kernel, $\bar{f}_i$ is the channel-wise mean of f_i, and the subscript $\text{group} = \mathcal{C}$ indicates depth-wise convolution (the number of groups equals the channel count $\mathcal{C}$).

In summary, if $\rho^{(j,k)} > \delta_1$, we use the mean-fusion rule in equation 3; otherwise, we apply the max–standard-deviation rule in equation 2. This mechanism automatically selects the more relevant spatial conditions and provides reliable conditioning even when the modalities conflict. Moreover, Gaussian smoothing suppresses the influence of early-stage noise, greatly improving the robustness and accuracy of the fusion process.

ChannelFusion. Before introducing ChannelFusion, we first revisit the limitations of PixFusion. Although PixFusion shows strong robustness to noise, it relies on a fixed-threshold fusion strategy that suffers from what we term *threshold degradation* in high-dimensional spaces. More precisely, as the feature dimensionality increases, the effectiveness of any fixed-threshold fusion progressively deteriorates.

For high-dimensional random vectors $\mathbf{X}, \mathbf{Y} \in \mathbb{R}^d$ with i.i.d. Gaussian components $\mathcal{N}(0, \sigma^2)$, their cosine similarity $\rho(\mathbf{X}, \mathbf{Y})$ satisfies

$$\mathbb{E}[\rho] = 0, \qquad \mathrm{Var}(\rho) = \frac{1}{d}. \tag{5}$$

(See Appendix A.2 for a proof.) This indicates that, in high dimensions, similarities between random vectors become increasingly concentrated around zero. Consequently, the pixel-level fixed-threshold fusion strategy becomes unreliable in high-dimensional regimes. Our empirical validation (Fig. 3a) confirms this phenomenon, showing a monotonic decrease in the proportion of features that satisfy the threshold as dimensionality grows.

To overcome this limitation, we propose ChannelFusion, a hybrid fusion strategy that adaptively combines *hard selection* and *soft fusion* based on a *standard-deviation consistency ratio*. This ratio leverages channel-level standard deviation statistics to quantify the relative condition strength of each modality, providing a dependable approach for feature fusion in high-dimensional embedding spaces.

Formally, consider the intermediate-layer features along the channel dimension. For the c-th channel, let $\hat{\sigma}_{1,c}, \hat{\sigma}_{2,c} \in \mathbb{R}$ denote the standard deviations of the two modalities. We define the standard-deviation consistency ratio

$$R_c = 1 - \frac{|\hat{\sigma}_{1,c} - \hat{\sigma}_{2,c}|}{\max\{\hat{\sigma}_{1,c}, \hat{\sigma}_{2,c}\}}, \tag{6}$$

which measures the relative consistency of conditional intensity between modalities for each channel ($R_c \in [0, 1]$).

Hard selection. When the consistency ratio R_c is below a predefined threshold δ_2, we adopt a *hard selection* strategy and keep only the feature from the modality with the larger standard deviation:

$$\hat{f}_c = f_{i^\star,c}, \qquad i^\star = \arg\max_i \hat{\sigma}_{i,c}. \tag{7}$$

This preserves the most informative features while discarding potentially noisy components.

Soft fusion. When $R_c \geq \delta_2$, we employ a *soft fusion* strategy that blends the features of both modalities using standard-deviation-proportional weights:

$$\hat{f}_c = \big(\Lambda_{1,c} + \Lambda_{2,c}\big)^{-1}\big(\Lambda_{1,c}\,\hat{f}_{1,c} + \Lambda_{2,c}\,\hat{f}_{2,c}\big). \tag{8}$$

Here $\Lambda_{i,c}$ denotes the precision (inverse covariance) of channel c in branch i. In practice we use the isotropic case $\Lambda_{i,c} = \lambda_{i,c}\mathbf{I}$, where the scalar $\lambda_{i,c}$ is proportional to the feature strength, $\lambda_{i,c} \propto \hat{\sigma}_{i,c}$. For numerical stability we set $\lambda_{i,c} = \frac{\hat{\sigma}_{i,c}}{\max(\hat{\sigma}_{1,c},\hat{\sigma}_{2,c})}$ (see Appendix A.3 for details). This weighted combination fully exploits the informative features from both branches.

This channel-wise adaptive strategy enables flexible feature fusion guided by conditional intensity, thereby improving image quality under multimodal conditions. By operating along the channel dimension rather than the spatial dimension, ChannelFusion effectively circumvents the high-dimensional threshold degradation problem and maximizes information retention.

3.3 FOREGROUND–BACKGROUND DECOUPLED KV-INJECTION

In multimodal settings with conflicting control signals, directly fusing intermediate-layer features often leads to ambiguous spatial conditioning, where different control inputs compete and the generator struggles to separate their contributions. We observe, however, that most generated images naturally exhibit a clear structural decomposition: a foreground object against a background scene. This observation suggests that treating foreground and background as distinct targets can reduce interference between competing conditions. Guided by this insight, we propose **Foreground–Background Decoupled KV-Injection**, which injects key–value pairs across ControlNet branches under text-derived attention masks to explicitly disentangle foreground and background representations.

Following prior works (Parmar et al., 2023; Liu et al., 2024; Mou et al., 2023; Hertz et al., 2024), we exploit the fact that cross-attention maps derived from the text prompt predominantly capture shape and structural cues. We therefore use these semantic cross-attention maps to automatically generate masks that distinguish foreground from background regions.

At denoising step $t{+}1$, within the backbone network's cross-attention layers, we aggregate all attention maps of resolution 256×77 (as in standard P2P practice) by averaging them to obtain 77 mask matrices of size 16×16, where 77 is the number of encoded prompt tokens (including padding). At step t, we select the averaged cross-attention map corresponding to the token most semantically relevant to the foreground object and, after post-processing, obtain the foreground mask M^f and its complementary background mask M^b.

Using these masks, we perform **region-isolated injection** inside the ControlNet self-attention layers: the key–value pairs of the foreground ControlNet are constrained to their designated regions via mask modulation, while the background ControlNet acts as the primary driver of global generation:

$$\begin{aligned}
&K_+ = [K_2 \oplus K_1], \quad V_+ = [V_2 \oplus V_1], \quad M_+ = [\mathbf{1} \oplus M^b], \\
&\mathrm{Attn}^f = \mathrm{softmax}\left(\frac{Q_2 K_1^\top}{\sqrt{d}} + \log M^f\right) V_1, \\
&\mathrm{Attn}^b = \mathrm{softmax}\left(\frac{Q_2 {K_+}^\top}{\sqrt{d}} + \log M_+\right) V_+, \\
&\hat{\mathrm{Attn}} = M^f \cdot \mathrm{Attn}^f + (1 - M^f) \cdot \mathrm{Attn}^b.
\end{aligned} \tag{9}$$

Here Q_1, K_1, V_1 denote the query, key, and value from the ControlNet conditioned on the foreground map, while Q_2, K_2, V_2 are from the background ControlNet; $\oplus$ indicates matrix concatenation. The final attention output $\hat{\mathrm{Attn}}$ ensures that each region retrieves information exclusively from its designated feature domain rather than from global features (see Fig. 2(b)).

In practice, KV-Injection is applied to all self-attention layers beginning at denoising step 5. This timing allows the early stages of the diffusion process to establish coarse structure before the injected signals guide finer foreground–background alignment, consistent with established denoising principles (Cao et al., 2023; Tewel et al., 2024).

Figure 4: Qualitative comparison under conflicting conditions. Prompts: (1) *"Teddy bear in red scarf on train windowsill."* (2) *"A woman stands in a golden rapeseed field."* (3) *"Po meditates beneath the ginkgo tree, watercolor style"*.

4 EXPERIMENT

4.1 IMPLEMENTATION DETAILS

All experiments are conducted on a single NVIDIA RTX 3090 GPU. We adopt Stable Diffusion v1.5 as the T2I backbone because of its rich ControlNet ecosystem and relatively low GPU-memory footprint. Our Cross-ControlNet is also compatible with DiT-based architectures, as demonstrated in Appendix A.5. Sampling uses the UniPC scheduler (Zhao et al., 2023b) with 50 steps and a classifier-free guidance scale of 7.5. The correlation threshold δ_1 and the consistency ratio threshold δ_2 are both set to a unified value $\delta = 0.7$. ChannelFusion is applied only in the final ControlNet layer, whereas PixFusion is used in all remaining layers. The kernels G_{κ_1} and G_{κ_2} are standard 3×3 Gaussian kernels normalized to unit sum.

Because no public dataset exists for *conflicting multi-condition* generation tasks, we construct a synthetic dataset based on COCO2017 (Lin et al., 2014). Following the procedure of the original ControlNet paper, we generate multiple conditional maps—Canny edges, depth maps, HED soft edges, OpenPose keypoints, and segmentation masks—using publicly available pre-trained models (Ranftl et al., 2020; Xie & Tu, 2015; Cao et al., 2019; Ravi et al., 2024). These maps are combined to form our synthetic dataset. For evaluation, 2,000 images are randomly sampled from the COCO2017 validation set, and BLIP-2 (Li et al., 2023a) is used to produce descriptive captions as text prompts. We compare Cross-ControlNet with state-of-the-art approaches including Multi-ControlNet (Zhang et al., 2023), Multi-Adapter (Mou et al., 2024), Cocktail (Hu et al., 2023), Uni-ControlNet (Zhao et al., 2023a), AnyControl (Sun et al., 2024), and MaxFusion (Nair et al., 2024).

4.2 QUALITATIVE EVALUATIONS

We present qualitative comparisons of Cross-ControlNet under both conflicting and complementary control conditions in Fig. 4 and Fig. 5, respectively. For conflicting conditions, where two control inputs impose contradictory spatial cues, we compare our method with Multi-Adapter, Multi-ControlNet, AnyControl, Uni-ControlNet, and MaxFusion. These baselines often fail to reconcile the conflicting signals: they typically introduce artifacts or degrade one of the intended structures. In contrast, Cross-ControlNet preserves both control cues and aligns more faithfully with the text prompt, producing sharp and semantically consistent results. For complementary conditions, where the control inputs reinforce each other, all methods generally generate plausible images. Nevertheless, our approach yields crisper object boundaries and more coherent backgrounds, demonstrating stronger alignment with both local and global structures. Overall, these results show that Cross-ControlNet achieves robust conditional consistency and high visual fidelity across both challenging conflicting scenarios and easier complementary ones. Additional qualitative examples are provided in Appendix A.6 for reference.

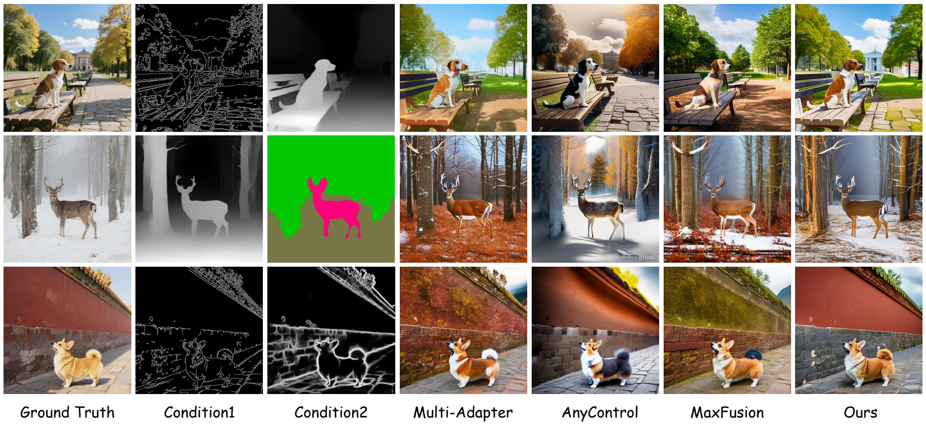

Figure 5: Qualitative comparison under complementary conditions. Prompts: (1) *"Brown-white dog on bench, blue sky."* (2) *"A deer in the snowy forest"* (3) *"A Corgi by red ancient wall."*.

Table 1: Quantitative results for **conflicting conditions**. ↑ means higher is better, ↓ lower is better. Best in **bold**, second-best underlined.

Method	Train-free	Pose, Seg			Pose, Depth		
		CLIP ↑	MSE-S ↓	mIoU-P ↑	CLIP ↑	MSE-D ↓	mIoU-P ↑
Multi-Adapter	✓	0.2738	0.2606	0.2911	0.2860	0.0516	0.2589
Multi-ControlNet	✓	**0.2999**	0.2282	0.3145	**0.2978**	0.0625	0.3150
AnyControl	×	0.2853	0.2522	0.2042	0.2638	**0.0338**	0.1519
Uni-ControlNet	×	0.2748	0.2310	0.1858	0.2695	0.0355	0.1445
Cocktail	×	0.2946	0.2037	0.1079	-	-	-
MaxFusion	✓	0.2945	0.2016	0.3528	0.2870	0.0498	0.3555
PixFusion (ours)	✓	0.2947	0.2004	0.3610	0.2887	0.0495	0.3583
+ChannelFusion (ours)	✓	0.2952	0.2009	0.3648	0.2865	0.0476	0.3618
Cross-ControlNet (ours)	✓	0.2978	**0.1983**	**0.3719**	0.2893	0.0456	**0.3671**

4.3 QUANTITATIVE EVALUATIONS

Analysis of Conflicting Conditions. The dataset constructed in Section 4.1 is insufficient for this analysis because it lacks cleanly separated foreground and background images. To address this limitation, we curated background images from BG-20K (Li et al., 2022) and generated pose maps for human-centric images selected from COCO2017, forming roughly 2,000 foreground–background pairs. For evaluation, we use CLIP-Score to measure text–image alignment and MSE and mIoU to quantify condition fidelity. As shown in Table 1, Cross-ControlNet consistently outperforms all other multimodal methods in condition fidelity while maintaining competitive text alignment. These results indicate that our model can reconcile complex combinations of conflicting conditions and produce high-quality outputs that remain faithful to both the text prompt and the control inputs.

Analysis of Complementary Conditions. Although Cross-ControlNet is primarily designed for conflicting-condition scenarios, it also performs strongly on complementary tasks. Here we employ the dataset introduced in Section 4.1 and follow the experimental setup of MaxFusion. Image quality is assessed with NIQE, text–image alignment with CLIP-Score, and condition fidelity with MSE and SSIM. As reported in Tables 2 and 3, Cross-ControlNet surpasses competing models overall, particularly in condition consistency and text–image alignment.

Table 2: complementary results (Hed, Seg)

Method	SSIM ↑	NIQE ↓	CLIP ↑	MSE-H ↓	MSE-S ↓
Multi-Adapter	0.2021	3.9493	0.2802	0.0746	0.1512
MaxFusion	0.2382	3.2499	0.2992	0.0766	0.1135
AnyControl	0.2251	4.8219	0.2989	**0.0554**	0.1046
Ours	**0.2404**	**3.2434**	**0.3005**	0.0736	**0.1008**

4.4 ABLATION STUDY

We conduct systematic ablation studies (Table 1) to assess the contribution of each core component in Cross-ControlNet. Three critical modules—PixFusion, ChannelFusion, and KV-Injection—are inte-

Table 3: Quantitative results for **complementary conditions**.

Method	Hed, Depth					Seg, Depth				
	SSIM ↑	NIQE ↓	CLIP ↑	MSE-H ↓	MSE-D ↓	SSIM ↑	NIQE ↓	CLIP ↑	MSE-S ↓	MSE-D ↓
Multi-Adapter	0.2411	3.5993	0.2962	0.0617	0.0218	0.2186	3.7793	0.2824	0.1384	0.0314
MaxFusion	0.2561	**3.3913**	0.2961	0.0615	0.0231	0.2358	3.4324	0.3022	0.1126	0.0257
AnyControl	0.2276	4.7683	**0.2986**	**0.0549**	0.0222	0.1975	4.5265	0.3014	0.1116	0.0241
Ours	**0.2622**	3.4153	0.2971	0.0570	**0.0212**	**0.2428**	**3.3887**	**0.3022**	**0.1105**	**0.0241**

grated incrementally, and we evaluate performance at each stage. Quantitative results show that each added component progressively improves conditional consistency while preserving textual alignment. In particular, even the standalone PixFusion configuration already surpasses the MaxFusion baseline in image synthesis metrics under conflicting scenarios. These findings highlight that the combined use of our proposed modules establishes state-of-the-art performance for controllable generation under conflicting conditions.

We also analyze the influence of the threshold δ on image synthesis. As illustrated in Fig. 6, when $\delta = 0$ the strategy degenerates to naive averaging, which weakens conditional information and yields images that are not faithful to the pose map. This effect persists until δ reaches roughly 0.6, where the images become more faithful to the conditions; however, some artifacts remain, such as faint "lines" in front of the person. At $\delta = 0.8$, the results achieve the best trade-off between conditional faithfulness and image quality. When $\delta = 1.0$, the boundary between the person and the mountain becomes noticeably unclear. Overall, we find that $\delta = 0.7$ provides a favorable balance between semantic coherence and detail preservation.

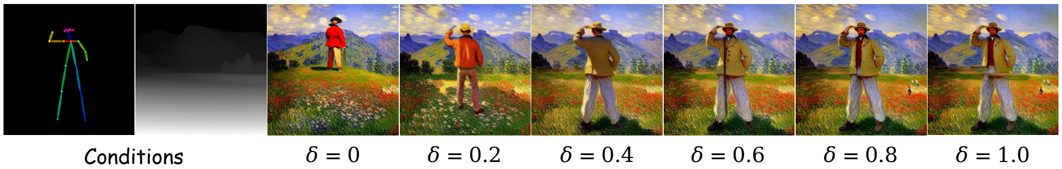

Figure 6: Ablation study on different δ values. The prompt is *"A man in a mountain, Monet style."*

Furthermore, we perform a fine-grained ablation of **KV-Injection** to determine its optimal insertion policy (see Appendix A.4). By varying both the starting denoising timestep and the first Cross-ControlNet block that receives injection, we find that beginning injection at an early but not initial timestep (timestep = 5) and starting from the earliest Cross-ControlNet block (layer = 0) yields the best trade-off: injecting at step 0 can slightly destabilize early denoising and harm perceptual scores, while very late injection reduces controllability; similarly, delaying the start-layer to deeper blocks weakens foreground–background propagation. These observations validate our default choices (starting timestep = 5, starting layer = 0).

5 CONCLUSION AND LIMITATION

We presented Cross-ControlNet, a training-free framework for multimodal conditional image generation that effectively handles both conflicting and complementary control signals. By integrating three key modules—PixFusion, ChannelFusion, and KV-Injection—our method mitigates challenges such as noise sensitivity and the degradation of fixed-threshold strategies in high-dimensional settings. These modules work synergistically to strengthen feature-fusion robustness, improve conditional consistency, and preserve semantic alignment with text prompts. Extensive experiments demonstrate that Cross-ControlNet delivers high-quality, harmonious images and consistently outperforms existing multimodal baselines. Looking ahead, we plan to refine these mechanisms and explore their extension to spatiotemporal domains such as video synthesis and 3D scene generation.

Limitation. Our framework relies on the availability of pre-trained single-condition ControlNets; it cannot directly support novel control modalities without such models. Combining multiple ControlNet branches also increases memory footprint and inference latency, which may limit deployment at very high resolutions or in real-time settings. Moreover, while our method improves consistency under conflicting conditions, extreme and mutually incompatible constraints can still lead to foreground-boundary artifacts or color bleeding.

REFERENCES

Yuval Alaluf, Daniel Garibi, Or Patashnik, Hadar Averbuch-Elor, and Daniel Cohen-Or. Cross-image attention for zero-shot appearance transfer. In *ACM SIGGRAPH 2024 conference papers*, pp. 1–12, 2024.

Omri Avrahami, Thomas Hayes, Oran Gafni, Sonal Gupta, Yaniv Taigman, Devi Parikh, Dani Lischinski, Ohad Fried, and Xi Yin. Spatext: Spatio-textual representation for controllable image generation. In *Proceedings of the IEEE/CVF conference on computer vision and pattern recognition*, pp. 18370–18380, 2023.

Yogesh Balaji, Seungjun Nah, Xun Huang, Arash Vahdat, Jiaming Song, Qinsheng Zhang, Karsten Kreis, Miika Aittala, Timo Aila, Samuli Laine, et al. ediff-i: Text-to-image diffusion models with an ensemble of expert denoisers. *arXiv preprint arXiv:2211.01324*, 2022.

Omer Bar-Tal, Lior Yariv, Yaron Lipman, and Tali Dekel. Multidiffusion: Fusing diffusion paths for controlled image generation. *arXiv preprint arXiv:2302.08113*, 2023.

Dina Bashkirova, José Lezama, Kihyuk Sohn, Kate Saenko, and Irfan Essa. Masksketch: Unpaired structure-guided masked image generation. In *Proceedings of the IEEE/CVF conference on computer vision and pattern recognition*, pp. 1879–1889, 2023.

Mingdeng Cao, Xintao Wang, Zhongang Qi, Ying Shan, Xiaohu Qie, and Yinqiang Zheng. Masactrl: Tuning-free mutual self-attention control for consistent image synthesis and editing. In *Proceedings of the IEEE/CVF international conference on computer vision*, pp. 22560–22570, 2023.

Zhe Cao, Gines Hidalgo, Tomas Simon, Shih-En Wei, and Yaser Sheikh. Openpose: Realtime multi-person 2d pose estimation using part affinity fields. *IEEE transactions on pattern analysis and machine intelligence*, 43(1):172–186, 2019.

Jingye Chen, Yupan Huang, Tengchao Lv, Lei Cui, Qifeng Chen, and Furu Wei. Textdiffuser: Diffusion models as text painters. *Advances in Neural Information Processing Systems*, 36: 9353–9387, 2023.

Jingye Chen, Yupan Huang, Tengchao Lv, Lei Cui, Qifeng Chen, and Furu Wei. Textdiffuser-2: Unleashing the power of language models for text rendering. In *European Conference on Computer Vision*, pp. 386–402. Springer, 2024a.

Junsong Chen, Chongjian Ge, Enze Xie, Yue Wu, Lewei Yao, Xiaozhe Ren, Zhongdao Wang, Ping Luo, Huchuan Lu, and Zhenguo Li. Pixart-σ: Weak-to-strong training of diffusion transformer for 4k text-to-image generation. In *European Conference on Computer Vision*, pp. 74–91. Springer, 2024b.

Jiwoo Chung, Sangeek Hyun, and Jae-Pil Heo. Style injection in diffusion: A training-free approach for adapting large-scale diffusion models for style transfer. In *Proceedings of the IEEE/CVF conference on computer vision and pattern recognition*, pp. 8795–8805, 2024.

Amir Hertz, Ron Mokady, Jay Tenenbaum, Kfir Aberman, Yael Pritch, and Daniel Cohen-Or. Prompt-to-prompt image editing with cross attention control. *arXiv preprint arXiv:2208.01626*, 2022.

Amir Hertz, Andrey Voynov, Shlomi Fruchter, and Daniel Cohen-Or. Style aligned image generation via shared attention. In *Proceedings of the IEEE/CVF Conference on Computer Vision and Pattern Recognition*, pp. 4775–4785, 2024.

Minghui Hu, Jianbin Zheng, Daqing Liu, Chuanxia Zheng, Chaoyue Wang, Dacheng Tao, and Tat-Jen Cham. Cocktail: Mixing multi-modality control for text-conditional image generation. In *Thirty-seventh Conference on Neural Information Processing Systems*, 2023.

Xuan Ju, Ailing Zeng, Chenchen Zhao, Jianan Wang, Lei Zhang, and Qiang Xu. Humansd: A native skeleton-guided diffusion model for human image generation. In *Proceedings of the IEEE/CVF International Conference on Computer Vision*, pp. 15988–15998, 2023.

Tero Karras, Miika Aittala, Timo Aila, and Samuli Laine. Elucidating the design space of diffusion-based generative models. *Advances in neural information processing systems*, 35:26565–26577, 2022.

Guandong Li. Training-free style consistent image synthesis with condition and mask guidance in e-commerce. *arXiv preprint arXiv:2409.04750*, 2024.

Jizhizi Li, Jing Zhang, Stephen J Maybank, and Dacheng Tao. Bridging composite and real: towards end-to-end deep image matting. *International Journal of Computer Vision*, 130(2):246–266, 2022.

Junnan Li, Dongxu Li, Silvio Savarese, and Steven Hoi. Blip-2: Bootstrapping language-image pre-training with frozen image encoders and large language models. In *International conference on machine learning*, pp. 19730–19742. PMLR, 2023a.

Yuheng Li, Haotian Liu, Qingyang Wu, Fangzhou Mu, Jianwei Yang, Jianfeng Gao, Chunyuan Li, and Yong Jae Lee. Gligen: Open-set grounded text-to-image generation. In *Proceedings of the IEEE/CVF conference on computer vision and pattern recognition*, pp. 22511–22521, 2023b.

Tsung-Yi Lin, Michael Maire, Serge Belongie, James Hays, Pietro Perona, Deva Ramanan, Piotr Dollár, and C Lawrence Zitnick. Microsoft coco: Common objects in context. In *European conference on computer vision*, pp. 740–755. Springer, 2014.

Bingyan Liu, Chengyu Wang, Tingfeng Cao, Kui Jia, and Jun Huang. Towards understanding cross and self-attention in stable diffusion for text-guided image editing. In *Proceedings of the IEEE/CVF conference on computer vision and pattern recognition*, pp. 7817–7826, 2024.

Sicheng Mo, Fangzhou Mu, Kuan Heng Lin, Yanli Liu, Bochen Guan, Yin Li, and Bolei Zhou. Freecontrol: Training-free spatial control of any text-to-image diffusion model with any condition. In *Proceedings of the IEEE/CVF Conference on Computer Vision and Pattern Recognition*, pp. 7465–7475, 2024.

Chong Mou, Xintao Wang, Jiechong Song, Ying Shan, and Jian Zhang. Dragondiffusion: Enabling drag-style manipulation on diffusion models. *arXiv preprint arXiv:2307.02421*, 2023.

Chong Mou, Xintao Wang, Liangbin Xie, Yanze Wu, Jian Zhang, Zhongang Qi, and Ying Shan. T2i-adapter: Learning adapters to dig out more controllable ability for text-to-image diffusion models. In *Proceedings of the AAAI conference on artificial intelligence*, volume 38, pp. 4296–4304, 2024.

Nithin Gopalakrishnan Nair, Jeya Maria Jose Valanarasu, and Vishal M Patel. Maxfusion: Plug&play multi-modal generation in text-to-image diffusion models. In *European Conference on Computer Vision*, pp. 93–110. Springer, 2024.

Gaurav Parmar, Krishna Kumar Singh, Richard Zhang, Yijun Li, Jingwan Lu, and Jun-Yan Zhu. Zero-shot image-to-image translation. In *ACM SIGGRAPH 2023 conference proceedings*, pp. 1–11, 2023.

Dustin Podell, Zion English, Kyle Lacey, Andreas Blattmann, Tim Dockhorn, Jonas Müller, Joe Penna, and Robin Rombach. Sdxl: Improving latent diffusion models for high-resolution image synthesis. *arXiv preprint arXiv:2307.01952*, 2023.

Can Qin, Shu Zhang, Ning Yu, Yihao Feng, Xinyi Yang, Yingbo Zhou, Huan Wang, Juan Carlos Niebles, Caiming Xiong, Silvio Savarese, et al. Unicontrol: A unified diffusion model for controllable visual generation in the wild. *arXiv preprint arXiv:2305.11147*, 2023.

René Ranftl, Katrin Lasinger, David Hafner, Konrad Schindler, and Vladlen Koltun. Towards robust monocular depth estimation: Mixing datasets for zero-shot cross-dataset transfer. *IEEE transactions on pattern analysis and machine intelligence*, 44(3):1623–1637, 2020.

Nikhila Ravi, Valentin Gabeur, Yuan-Ting Hu, Ronghang Hu, Chaitanya Ryali, Tengyu Ma, Haitham Khedr, Roman Rädle, Chloe Rolland, Laura Gustafson, et al. Sam 2: Segment anything in images and videos. *arXiv preprint arXiv:2408.00714*, 2024.

Robin Rombach, Andreas Blattmann, Dominik Lorenz, Patrick Esser, and Björn Ommer. High-resolution image synthesis with latent diffusion models. In *Proceedings of the IEEE/CVF conference on computer vision and pattern recognition*, pp. 10684–10695, 2022.

Chitwan Saharia, William Chan, Saurabh Saxena, Lala Li, Jay Whang, Emily L Denton, Kamyar Ghasemipour, Raphael Gontijo Lopes, Burcu Karagol Ayan, Tim Salimans, et al. Photorealistic text-to-image diffusion models with deep language understanding. *Advances in neural information processing systems*, 35:36479–36494, 2022.

Shikun Sun, Min Zhou, Zixuan Wang, Xubin Li, Tiezheng Ge, Zijie Ye, Xiaoyu Qin, Junliang Xing, Bo Zheng, and Jia Jia. Minimal impact controlnet: Advancing multi-controlnet integration. *arXiv preprint arXiv:2506.01672*, 2025.

Yanan Sun, Yanchen Liu, Yinhao Tang, Wenjie Pei, and Kai Chen. Anycontrol: create your artwork with versatile control on text-to-image generation. In *European Conference on Computer Vision*, pp. 92–109. Springer, 2024.

Zhenxiong Tan, Songhua Liu, Xingyi Yang, Qiaochu Xue, and Xinchao Wang. Ominicontrol: Minimal and universal control for diffusion transformer. *arXiv preprint arXiv:2411.15098*, 2024.

Yoad Tewel, Omri Kaduri, Rinon Gal, Yoni Kasten, Lior Wolf, Gal Chechik, and Yuval Atzmon. Training-free consistent text-to-image generation. *ACM Transactions on Graphics (TOG)*, 43(4): 1–18, 2024.

Narek Tumanyan, Michal Geyer, Shai Bagon, and Tali Dekel. Plug-and-play diffusion features for text-driven image-to-image translation. In *Proceedings of the IEEE/CVF conference on computer vision and pattern recognition*, pp. 1921–1930, 2023.

Bingyuan Wang, Qifeng Chen, and Zeyu Wang. Diffusion-based visual art creation: A survey and new perspectives. *ACM Computing Surveys*, 57(10):1–37, 2025a.

Haoxuan Wang, Jinlong Peng, Qingdong He, Hao Yang, Ying Jin, Jiafu Wu, Xiaobin Hu, Yanjie Pan, Zhenye Gan, Mingmin Chi, et al. Unicombine: Unified multi-conditional combination with diffusion transformer. *arXiv preprint arXiv:2503.09277*, 2025b.

Luozhou Wang, Guibao Shen, Wenhang Ge, Guangyong Chen, Yijun Li, and Yingcong Chen. Text-anchored score composition: Tackling condition misalignment in text-to-image diffusion models. In *European Conference on Computer Vision*, pp. 21–37. Springer, 2024.

Zhendong Wang, Jianmin Bao, Shuyang Gu, Dong Chen, Wengang Zhou, and Houqiang Li. Designdiffusion: High-quality text-to-design image generation with diffusion models. In *Proceedings of the Computer Vision and Pattern Recognition Conference*, pp. 20906–20915, 2025c.

Jinheng Xie, Yuexiang Li, Yawen Huang, Haozhe Liu, Wentian Zhang, Yefeng Zheng, and Mike Zheng Shou. Boxdiff: Text-to-image synthesis with training-free box-constrained diffusion. In *Proceedings of the IEEE/CVF International Conference on Computer Vision*, pp. 7452–7461, 2023.

Saining Xie and Zhuowen Tu. Holistically-nested edge detection. In *Proceedings of the IEEE international conference on computer vision*, pp. 1395–1403, 2015.

Zeyue Xue, Guanglu Song, Qiushan Guo, Boxiao Liu, Zhuofan Zong, Yu Liu, and Ping Luo. Raphael: Text-to-image generation via large mixture of diffusion paths. *Advances in Neural Information Processing Systems*, 36:41693–41706, 2023.

Lvmin Zhang, Anyi Rao, and Maneesh Agrawala. Adding conditional control to text-to-image diffusion models. In *Proceedings of the IEEE/CVF international conference on computer vision*, pp. 3836–3847, 2023.

Shihao Zhao, Dongdong Chen, Yen-Chun Chen, Jianmin Bao, Shaozhe Hao, Lu Yuan, and Kwan-Yee K Wong. Uni-controlnet: All-in-one control to text-to-image diffusion models. *Advances in Neural Information Processing Systems*, 36:11127–11150, 2023a.

Wenliang Zhao, Lujia Bai, Yongming Rao, Jie Zhou, and Jiwen Lu. Unipc: A unified predictor-corrector framework for fast sampling of diffusion models. *Advances in Neural Information Processing Systems*, 36:49842–49869, 2023b.

Guangcong Zheng, Xianpan Zhou, Xuewei Li, Zhongang Qi, Ying Shan, and Xi Li. Layoutdiffusion: Controllable diffusion model for layout-to-image generation. In *Proceedings of the IEEE/CVF Conference on Computer Vision and Pattern Recognition*, pp. 22490–22499, 2023.

Tianrui Zhu, Shiyi Zhang, Jiawei Shao, and Yansong Tang. Kv-edit: Training-free image editing for precise background preservation. *arXiv preprint arXiv:2502.17363*, 2025.

A APPENDIX

A.1 STATEMENT

LLM Usage Statement. This paper's ideas, methodology, code, and experimental design were entirely conceived and implemented by the authors. Large Language Models (OpenAI GPT-5) were used only for minor English language polishing of the manuscript; no model output contributed to the research content itself.

Ethics Statement. Our work focuses on improving controllable text-to-image generation. All datasets used in experiments are publicly available and contain only non-personal, non-sensitive images. The proposed method does not introduce additional privacy, safety, or fairness concerns beyond those already present in standard diffusion models.

Reproducibility Statement. We release source code at https://anonymous.4open.science/r/Cross-ControlNet-6C5F. All implementation details, hyperparameters, and experimental settings are provided in the main text and appendix to facilitate full replication of our results.

A.2 COSINE SIMILARITY OF INDEPENDENT GAUSSIANS

Let $\mathbf{X}, \mathbf{Y} \in \mathbb{R}^d$ be two independent random vectors with i.i.d. components $X_i, Y_i \sim \mathcal{N}(0, \sigma^2)$. Define the cosine similarity

$$\rho = \frac{\mathbf{X} \cdot \mathbf{Y}}{\|\mathbf{X}\| \, \|\mathbf{Y}\|}. \tag{10}$$

It is well known that for a Gaussian vector $\mathbf{X} \sim \mathcal{N}(0, \sigma^2 I_d)$, the direction $U = \mathbf{X}/\|\mathbf{X}\|$ is independent of the radius $\|\mathbf{X}\|$ and is uniformly distributed on the unit sphere S^{d-1}. The same holds for $\mathbf{Y}$. Hence we can write

$$\rho = U \cdot V, \tag{11}$$

where $U, V \in S^{d-1}$ are independent and uniformly distributed on the sphere.

By symmetry, the mean of each coordinate of V is zero, which implies $\mathbb{E}[V] = 0$. Therefore

$$\mathbb{E}[\rho] = \mathbb{E}[U \cdot V] = \mathbb{E}\big[U \cdot \mathbb{E}[V]\big] = 0. \tag{12}$$

To compute the variance, observe that

$$\mathrm{Var}(\rho) = \mathbb{E}[\rho^2] = \mathbb{E}[(U \cdot V)^2]. \tag{13}$$

Since U and V are independent, we can condition on U:

$$\mathbb{E}[(U \cdot V)^2] = \mathbb{E}\left[\mathbb{E}[(U \cdot V)^2 \mid U]\right]. \tag{14}$$

For fixed U, we have

$$\mathbb{E}[(U \cdot V)^2 \mid U] = \mathbb{E}[U^\top (V V^\top) U \mid U] = U^\top \, \mathbb{E}[V V^\top] \, U. \tag{15}$$

Rotational invariance of the uniform distribution on the sphere implies that $\mathbb{E}[VV^\top]$ must be a scalar multiple of the identity, say $\mathbb{E}[VV^\top] = cI_d$. Taking traces gives

$$cd = \mathrm{tr}(cI_d) = \mathrm{tr}\big(\mathbb{E}[VV^\top]\big) = \mathbb{E}[\|V\|^2] = 1, \tag{16}$$

hence $c = 1/d$. Therefore

$$\mathbb{E}[(U \cdot V)^2 \mid U] = U^\top \left(\tfrac{1}{d} I_d\right) U = \tfrac{1}{d}\|U\|^2 = \tfrac{1}{d}. \tag{17}$$

Since this conditional expectation is constant (does not depend on U), we have

$$\mathbb{E}[\rho^2] = \mathbb{E}\left[\tfrac{1}{d}\right] = \tfrac{1}{d}, \tag{18}$$

and consequently

$$\mathbb{E}[\rho] = 0, \qquad \mathrm{Var}(\rho) = \frac{1}{d}. \tag{19}$$

This completes the proof of Formula 5. Notably, the result does not depend on the variance σ^2, but only on the rotational symmetry of the Gaussian distribution.

A.3 DERIVATION OF CHANNELFUSION VIA VARIATIONAL INFERENCE

We derive the ChannelFusion method using variational inference and evidence lower bound (ELBO) maximization. For a fixed channel index c, we consider two feature maps $\mathbf{k}_1, \mathbf{k}_2 \in \mathbb{R}^{H \times W}$, which we vectorize to treat as vectors in $\mathbb{R}^{HW}$.

Notation clarification: in the main text, these correspond to the channel-specific features $\mathbf{f}_{1,c}$ and $\mathbf{f}_{2,c}$, i.e., $\mathbf{k}_1 = \mathbf{f}_{1,c}$ and $\mathbf{k}_2 = \mathbf{f}_{2,c}$. We assume that the actual semantic feature is $\mathbf{y}$, which is unobservable, while the observable features are $\mathbf{k}_1$ and $\mathbf{k}_2$. Since $\mathbf{y}$ has no exact observed value, we can only use $q(\mathbf{y})$ to describe its distribution and estimate $q(\mathbf{y})$ through $\mathbf{k}_1$ and $\mathbf{k}_2$.

A.3.1 GENERATIVE MODEL AND VARIATIONAL SETUP

To enhance robustness, we assume that in the absence of any observed values, $\mathbf{y}$ generally follows a Gaussian distribution $p(\mathbf{y})$. Furthermore, since $\mathbf{k}_1$ and $\mathbf{k}_2$ are observations from potentially biased channels, they inevitably deviate from $\mathbf{y}$. We model this observation bias using a diffusion process, where $\mathbf{k}_1$ and $\mathbf{k}_2$ follow Gaussian distributions $p(\mathbf{k}_1|\mathbf{y})$ and $p(\mathbf{k}_2|\mathbf{y})$ with $\mathbf{y}$ as the mean and $\mathbf{\Sigma}_1$, $\mathbf{\Sigma}_2$ (representing the respective channel biases) as the covariance matrices:

$$\begin{gathered} p(\mathbf{y}) = \mathcal{N}(\mathbf{y}|\boldsymbol{\mu}_0, \mathbf{\Sigma}_0) \\ p(\mathbf{k}_i|\mathbf{y}) = \mathcal{N}(\mathbf{k}_i|\mathbf{y}, \mathbf{\Sigma}_i), \quad i = 1, 2 \end{gathered} \tag{20}$$

Similarly, we also use a Gaussian distribution to model the estimated $q(\mathbf{y})$.

$$q(\mathbf{y}) = \mathcal{N}(\mathbf{y}|\boldsymbol{\mu}_\theta, \mathbf{\Sigma}_y) \tag{21}$$

where $\boldsymbol{\mu}_\theta$ is the mean and $\mathbf{\Sigma}_y$ is the covariance matrix.

A.3.2 EVIDENCE LOWER BOUND (ELBO)

We perform variational inference by maximizing the Evidence Lower Bound (ELBO) of $q(\mathbf{y})$ given the two observations $\mathbf{k}_1$ and $\mathbf{k}_2$, where the ELBO $\mathcal{L}(q)$ is defined as:

$$\mathcal{L}(q) = \mathbb{E}_{q(\mathbf{y})}\left[\log \frac{p(\mathbf{y}, \mathbf{k}_1, \mathbf{k}_2)}{q(\mathbf{y})}\right] = \mathbb{E}_{q(\mathbf{y})}\left[\log \frac{p(\mathbf{k}_1, \mathbf{k}_2|\mathbf{y})p(\mathbf{y})}{q(\mathbf{y})}\right] \tag{22}$$

A.3.3 DETAILED DERIVATION OF THE ELBO AND OPTIMAL PARAMETERS

Substituting the Gaussian densities into the ELBO and letting $D = HW$ denote the dimensionality, we have:

$$\begin{aligned} \mathcal{L}(q) &= \int \mathcal{N}(\mathbf{y}|\boldsymbol{\mu}_\theta, \mathbf{\Sigma}_y) \log \left(\frac{\mathcal{N}(\mathbf{y}|\boldsymbol{\mu}_0, \mathbf{\Sigma}_0) \prod_{i=1}^{2} \mathcal{N}(\mathbf{k}_i|\mathbf{y}, \mathbf{\Sigma}_i)}{\mathcal{N}(\mathbf{y}|\boldsymbol{\mu}_\theta, \mathbf{\Sigma}_y)} \right) d\mathbf{y} \\ &= \int \mathcal{N}(\mathbf{y}|\boldsymbol{\mu}_\theta, \mathbf{\Sigma}_y) \\ &\quad \log \left(\frac{\frac{1}{(2\pi)^{D/2}|\mathbf{\Sigma}_0|^{1/2}} e^{-\frac{1}{2}(\mathbf{y}-\boldsymbol{\mu}_0)^\top \mathbf{\Sigma}_0^{-1}(\mathbf{y}-\boldsymbol{\mu}_0)} \prod_{i=1}^{2} \frac{1}{(2\pi)^{D/2}|\mathbf{\Sigma}_i|^{1/2}} e^{-\frac{1}{2}(\mathbf{k}_i-\mathbf{y})^\top \mathbf{\Sigma}_i^{-1}(\mathbf{k}_i-\mathbf{y})}}{\frac{1}{(2\pi)^{D/2}|\mathbf{\Sigma}_y|^{1/2}} e^{-\frac{1}{2}(\mathbf{y}-\boldsymbol{\mu}_\theta)^\top \mathbf{\Sigma}_y^{-1}(\mathbf{y}-\boldsymbol{\mu}_\theta)}} \right) d\mathbf{y} \end{aligned} \tag{23}$$

Simplifying the logarithm, we obtain:

$$\begin{aligned} \mathcal{L}(q) = \int \mathcal{N}(\mathbf{y}|\boldsymbol{\mu}_\theta, \mathbf{\Sigma}_y) \Bigg[& \log|\mathbf{\Sigma}_y|^{1/2} - \log|\mathbf{\Sigma}_0|^{1/2} - \sum_{i=1}^{2} \log\big((2\pi)^{D/2}|\mathbf{\Sigma}_i|^{1/2}\big) \\ & - \tfrac{1}{2}\Big((\mathbf{y}-\boldsymbol{\mu}_0)^\top \mathbf{\Sigma}_0^{-1}(\mathbf{y}-\boldsymbol{\mu}_0) + \sum_{i=1}^{2}(\mathbf{k}_i-\mathbf{y})^\top \mathbf{\Sigma}_i^{-1}(\mathbf{k}_i-\mathbf{y}) \\ & - (\mathbf{y}-\boldsymbol{\mu}_\theta)^\top \mathbf{\Sigma}_y^{-1}(\mathbf{y}-\boldsymbol{\mu}_\theta)\Big)\Bigg] d\mathbf{y}. \end{aligned} \tag{24}$$

Since $\mathcal{N}(\mathbf{y}|\boldsymbol{\mu}_\theta, \boldsymbol{\Sigma}_y)$ is a probability density, the terms independent of $\mathbf{y}$ can be moved outside the integral. The integral of $\mathcal{N}(\mathbf{y}|\boldsymbol{\mu}_\theta, \boldsymbol{\Sigma}_y)$ is 1, leading to:

$$\begin{aligned}\mathcal{L}(q) = \tfrac{1}{2}\log|\boldsymbol{\Sigma}_y| - \tfrac{1}{2}\log|\boldsymbol{\Sigma}_0| - \sum_{i=1}^{2}\tfrac{1}{2}\log\big((2\pi)^D|\boldsymbol{\Sigma}_i|\big) \\ - \tfrac{1}{2}\int q(\mathbf{y})\Big[(\mathbf{y}-\boldsymbol{\mu}_0)^\top\boldsymbol{\Sigma}_0^{-1}(\mathbf{y}-\boldsymbol{\mu}_0) + \sum_{i=1}^{2}(\mathbf{k}_i-\mathbf{y})^\top\boldsymbol{\Sigma}_i^{-1}(\mathbf{k}_i-\mathbf{y}) \\ - (\mathbf{y}-\boldsymbol{\mu}_\theta)^\top\boldsymbol{\Sigma}_y^{-1}(\mathbf{y}-\boldsymbol{\mu}_\theta)\Big]d\mathbf{y}.\end{aligned} \tag{25}$$

We now expand the quadratic forms and use the properties of expectations under $q(\mathbf{y})$: $\mathbb{E}[\mathbf{y}] = \boldsymbol{\mu}_\theta$ and $\mathbb{E}[\mathbf{y}\mathbf{y}^\top] = \boldsymbol{\Sigma}_y + \boldsymbol{\mu}_\theta\boldsymbol{\mu}_\theta^\top$.

$$\begin{aligned}\mathbb{E}[(\mathbf{y}-\boldsymbol{\mu}_0)^\top\boldsymbol{\Sigma}_0^{-1}(\mathbf{y}-\boldsymbol{\mu}_0)] &= (\boldsymbol{\mu}_\theta-\boldsymbol{\mu}_0)^\top\boldsymbol{\Sigma}_0^{-1}(\boldsymbol{\mu}_\theta-\boldsymbol{\mu}_0) + \mathrm{tr}(\boldsymbol{\Sigma}_0^{-1}\boldsymbol{\Sigma}_y) \\ \mathbb{E}[(\mathbf{k}_i-\mathbf{y})^\top\boldsymbol{\Sigma}_i^{-1}(\mathbf{k}_i-\mathbf{y})] &= (\mathbf{k}_i-\boldsymbol{\mu}_\theta)^\top\boldsymbol{\Sigma}_i^{-1}(\mathbf{k}_i-\boldsymbol{\mu}_\theta) + \mathrm{tr}(\boldsymbol{\Sigma}_i^{-1}\boldsymbol{\Sigma}_y) \\ \mathbb{E}[(\mathbf{y}-\boldsymbol{\mu}_\theta)^\top\boldsymbol{\Sigma}_y^{-1}(\mathbf{y}-\boldsymbol{\mu}_\theta)] &= \mathrm{tr}(\boldsymbol{\Sigma}_y^{-1}\boldsymbol{\Sigma}_y) = D\end{aligned} \tag{26}$$

Substituting these expectations back into the ELBO, we get the final expression:

$$\begin{aligned}\mathcal{L}(q) = \frac{1}{2}\log|\boldsymbol{\Sigma}_y| - \frac{1}{2}\log|\boldsymbol{\Sigma}_0| - \sum_{i=1}^{2}\frac{1}{2}\log\left((2\pi)^D|\boldsymbol{\Sigma}_i|\right) - \frac{D}{2} \\ - \frac{1}{2}\left[(\boldsymbol{\mu}_\theta-\boldsymbol{\mu}_0)^\top\boldsymbol{\Sigma}_0^{-1}(\boldsymbol{\mu}_\theta-\boldsymbol{\mu}_0) + \mathrm{tr}(\boldsymbol{\Sigma}_0^{-1}\boldsymbol{\Sigma}_y)\right] \\ - \frac{1}{2}\sum_{i=1}^{2}\left[(\mathbf{k}_i-\boldsymbol{\mu}_\theta)^\top\boldsymbol{\Sigma}_i^{-1}(\mathbf{k}_i-\boldsymbol{\mu}_\theta) + \mathrm{tr}(\boldsymbol{\Sigma}_i^{-1}\boldsymbol{\Sigma}_y)\right]\end{aligned} \tag{27}$$

Optimal Variational Parameters

To find the optimal variational parameters, we maximize the ELBO with respect to $\boldsymbol{\mu}_\theta$.

Optimal Mean $\boldsymbol{\mu}_\theta^*$: The terms containing $\boldsymbol{\mu}_\theta$ are:

$$-\frac{1}{2}(\boldsymbol{\mu}_\theta-\boldsymbol{\mu}_0)^\top\boldsymbol{\Sigma}_0^{-1}(\boldsymbol{\mu}_\theta-\boldsymbol{\mu}_0) - \frac{1}{2}\sum_{i=1}^{2}(\mathbf{k}_i-\boldsymbol{\mu}_\theta)^\top\boldsymbol{\Sigma}_i^{-1}(\mathbf{k}_i-\boldsymbol{\mu}_\theta) \tag{28}$$

Taking the gradient with respect to $\boldsymbol{\mu}_\theta$ and setting it to zero:

$$\begin{aligned}\nabla_{\boldsymbol{\mu}_\theta}\mathcal{L} &= -\boldsymbol{\Sigma}_0^{-1}(\boldsymbol{\mu}_\theta-\boldsymbol{\mu}_0) + \sum_{i=1}^{2}\boldsymbol{\Sigma}_i^{-1}(\mathbf{k}_i-\boldsymbol{\mu}_\theta) = 0 \\ &= -\left(\boldsymbol{\Sigma}_0^{-1} + \sum_{i=1}^{2}\boldsymbol{\Sigma}_i^{-1}\right)\boldsymbol{\mu}_\theta + \left(\boldsymbol{\Sigma}_0^{-1}\boldsymbol{\mu}_0 + \sum_{i=1}^{2}\boldsymbol{\Sigma}_i^{-1}\mathbf{k}_i\right) = 0\end{aligned} \tag{29}$$

Solving for $\boldsymbol{\mu}_\theta$ gives the optimal mean:

$$\boxed{\boldsymbol{\mu}_\theta^* = \left(\boldsymbol{\Sigma}_0^{-1} + \boldsymbol{\Sigma}_1^{-1} + \boldsymbol{\Sigma}_2^{-1}\right)^{-1}\left(\boldsymbol{\Sigma}_0^{-1}\boldsymbol{\mu}_0 + \boldsymbol{\Sigma}_1^{-1}\mathbf{k}_1 + \boldsymbol{\Sigma}_2^{-1}\mathbf{k}_2\right)} \tag{30}$$

A.3.4 SPECIALIZATION TO CHANNELFUSION

For practical implementation in ChannelFusion, we make the following simplifying assumptions: 1. **Isotropic Covariances:** $\boldsymbol{\Sigma}_i^{-1} = \lambda_i\mathbf{I}$, where $\mathbf{I}$ is the identity matrix. 2. **Uninformative Prior:** $\lambda_0 \to 0$, which implies $\boldsymbol{\Sigma}_0^{-1} \to \mathbf{0}$. 3. **Precision Proportional to Feature Strength:** $\lambda_i = \frac{\hat{\sigma}_{i,c}}{\max(\hat{\sigma}_{1,c},\hat{\sigma}_{2,c})}$, where $\hat{\sigma}_{i,c}$ represents the feature strength of the c-th channel in the i-th feature map.

Remark. Here the quantity $\hat{\sigma}_{i,c}$ is the empirical standard deviation of pixel values *within* the c-th channel of the feature map, obtained by treating the channel elements as samples. It serves only as

Table 4: Ablation on the starting timestep and starting layer under **conflicting conditions**.

Variant	Pose, Seg			Pose, Depth		
	CLIP ↑	MSE-s ↓	mIoU-p ↑	CLIP ↑	MSE-d ↓	mIoU-p ↑
Cross-ControlNet (step-0, layer-0)	0.2976	0.2003	0.3741	0.2898	0.0478	0.3587
Cross-ControlNet (step-5, layer-0)	0.2978	0.1983	0.3719	0.2893	0.0456	0.3671
Cross-ControlNet (step-10, layer-0)	0.2968	0.1981	0.3712	0.2862	0.0447	0.3647
Cross-ControlNet (step-15, layer-0)	0.2956	0.1989	0.3725	0.2863	0.0449	0.3657
Cross-ControlNet (step-20, layer-0)	0.2952	0.2011	0.3736	0.2862	0.0462	0.3641
Cross-ControlNet (layer-0, step-5)	0.2978	0.1983	0.3719	0.2893	0.0456	0.3671
Cross-ControlNet (layer-2, step-5)	0.2974	0.2068	0.3703	0.2877	0.0483	0.3680
Cross-ControlNet (layer-4, step-5)	0.2970	0.2072	0.3691	0.2902	0.0448	0.3653

a proxy for the amount of useful information carried by that channel and should not be confused with the observation–noise variance in the Gaussian generative model. Accordingly, in practice we *instantiate* the Bayesian "precision" weights λ_i via a monotonic proxy of channel strength, setting $\lambda_i \propto \hat{\sigma}_{i,c}$. This serves as a practical surrogate for the (typically unavailable) inverse noise variance and does not alter the underlying model.

Substituting these assumptions into the optimal mean equation 30:

$$\begin{aligned} \boldsymbol{\mu}_\theta^* &= (\lambda_0\mathbf{I} + \lambda_1\mathbf{I} + \lambda_2\mathbf{I})^{-1}(\lambda_0\mathbf{I}\boldsymbol{\mu}_0 + \lambda_1\mathbf{I}\mathbf{k}_1 + \lambda_2\mathbf{I}\mathbf{k}_2) \\ &\approx (\lambda_1\mathbf{I} + \lambda_2\mathbf{I})^{-1}(\lambda_1\mathbf{k}_1 + \lambda_2\mathbf{k}_2) \quad (\text{since } \lambda_0 \to 0) \\ &= \frac{\lambda_1}{\lambda_1+\lambda_2}\mathbf{k}_1 + \frac{\lambda_2}{\lambda_1+\lambda_2}\mathbf{k}_2 \end{aligned} \tag{31}$$

This gives us the ChannelFusion soft fusion rule:

$$\boxed{\boldsymbol{\mu}_\theta^* = \frac{\lambda_1}{\lambda_1+\lambda_2}\mathbf{k}_1 + \frac{\lambda_2}{\lambda_1+\lambda_2}\mathbf{k}_2} \tag{32}$$

The hard selection rule is obtained in the limit where one λ_i dominates the other (effectively setting the smaller λ to zero), which corresponds to complete certainty in one feature map.

A.3.5 DISCUSSION

This derivation shows that ChannelFusion can be interpreted as performing variational Bayesian inference under a conjugate Gaussian generative model. The optimal fusion rule 32 is derived by maximizing the ELBO, providing a principled justification for the weighted average of feature maps. The precision parameters λ_i act as reliable estimates of the useful information content in each feature map, determining their contribution to the fused output. The assumptions of isotropy and an uninformative prior make the method computationally efficient and suitable for integration into deep neural networks.

A.4 ADDITIONAL ABLATION STUDIES

We further examine the control policy of KV-Injection by varying (1) the starting timestep in the denoising process and (2) the starting layer within Cross-ControlNet at which injection begins. Here, we explicitly clarify that the term *starting layer* denotes the index of the first Cross-ControlNet block that receives KV-Injection; injection is applied from this block onward to subsequent blocks in the network. This distinction is important because earlier vs. later start layers determine how much of the feature hierarchy is exposed to the injected key–value information.

All other components are kept identical to the main experiment; only the KV-Injection settings are modified.

The upper block of Table 4 reports the results when the starting layer is fixed to 0 and the starting timestep is varied. Intuitively, an earlier timestep gives the injected correlation signal more opportunity

Figure 7: Visual comparison under varying threshold δ. For small δ (< 0.4) the generated image is not sufficiently faithful to the given foreground/background conditions. As δ increases, adherence gradually improves; however, for large δ (> 0.6) a distinct white rim appears between foreground and background. Although such results are extremely faithful, the rim destroys photorealism and breaks the overall harmony. Prompt: " photo of a cowboy riding a black horse in a street, harmoniously".

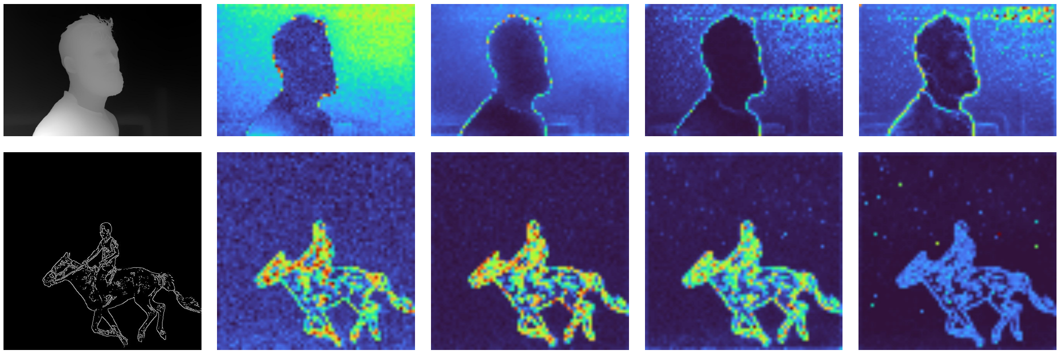

Figure 8: Spatial variance maps of image tokens processed by the MM-DiT blocks of FLUX.1-dev ControlNets. These variance maps also reflect the strength of the conditional information.

to shape the denoising trajectory, whereas a very late injection fails to sufficiently influence the reconstruction. Empirically, starting too early (e.g., step 0) can slightly destabilize the early denoising dynamics and degrade perceptual scores, while starting too late reduces controllability. A starting timestep of 5 therefore provides a favorable trade-off between influence and stability.

In the lower block, we fix the starting timestep at 5 and vary the starting layer. Injection beginning at layer 0 yields the best performance: by introducing the conditioning signal at the earliest Cross-ControlNet block, the guidance can propagate through the full depth of the module and influence both low- and high-level features. Delaying the start to deeper layers reduces this propagation, leaving earlier features effectively unconditioned and weakening foreground–background alignment; this manifests as lower scores in the reported metrics.

Overall, these ablations validate the default choice used in the main paper (starting timestep = 5, starting layer = 0). They also show that KV-Injection is reasonably robust across a range of timesteps and start-layer choices, but attains the strongest and most consistent control when initialized early in both the denoising schedule and the Cross-ControlNet hierarchy.

A.5 CROSS-ARCHITECTURE GENERALIZATION: U-NET → DIT (FLUX)

Our method is not limited to U-Net architectures; it can be seamlessly transferred to diffusion-transformer models such as FLUX. We conducted tests using FLUX.1-dev with 28 sampling steps, and the classifier-free guidance was set to 3.5. The correlation threshold δ was set to 0.50 (see Fig. 7 for visual examples). For the KV-Injection part, as the foreground mask was not readily available, we opted for simplicity by setting it to all ones by default. KV-Injection began to take effect from step 3 onward. Beyond these changes, the model maintained the same settings as in the main paper.

Although FLUX replaces the convolutional U-Net backbone with a DiT-style Transformer architecture that relies on global self-attention, the proposed cross-modal correlation and KV-Injection remain entirely attention-based and therefore require no additional architectural tuning. As further evidenced in Fig. 8, the feature variance within FLUX likewise reveals clear intensity patterns, confirming that our correlation-based mechanism can exploit informative representations despite the architectural change. In practice, the injection of correlation-guided key–value pairs integrates smoothly into the

Transformer blocks, demonstrating that the method is agnostic to whether the latent features originate from convolutional layers or purely transformer-based representations.

Qualitatively, we observe that FLUX produces sharper fine-grained textures and more globally consistent structures compared to its U-Net counterparts, while maintaining the same level of foreground–background controllability (see Figs. 9 and Figs. 10). This indicates that Cross-ControlNet is robust to architectural changes and can preserve the intended conditioning signals even when the underlying diffusion backbone shifts from U-Net to DiT.

Naturally, the method—originally designed for U-Net—also performs well on the U-Net-based SDXL model; we omit these results for brevity.

A.6 ADDITIONAL QUALITATIVE RESULTS

To further illustrate the effectiveness of our Cross-ControlNet when applied to the U-Net–based Stable Diffusion v1.5, we provide additional qualitative samples in Fig. 11 and Fig. 12. These examples cover a diverse set of foreground–background configurations and artistic styles: single-object foregrounds (e.g., an astronaut on the moon, a sailing boat on a calm lake, a lighthouse on a rocky cliff, a cherry blossom tree with Mt. Fuji, a desert cactus, or a canyon hiker), everyday still-life scenes (e.g., a vintage typewriter or camera on a wooden desk, or a macro glass terrarium), street and architectural compositions (e.g., a classic red telephone booth or sunglasses on a marble column framing the Parthenon), natural landscapes (e.g., a quiet snowy village or a dawn pasture with a shepherd), cultural scenes (e.g., a Chinese lion dance), and illustrative artworks (e.g., a cartoon dog and cat in minimal line-art or a pastel origami fox). The gallery spans rendering styles from photorealistic to minimal line-art and painterly oil textures. Across these variations, Cross-ControlNet consistently preserves the intended conditioning signals (foreground shape and background layout), generates high-fidelity details, and maintains coherent foreground–background separation (see Fig. 11 and Fig. 12). These supplementary results further corroborate the robustness and versatility of our method beyond the representative cases shown in the main paper.

Ghibli 2D: teen witch on broom over Eiffel Tower. *WALL-E is in the supermarket.*

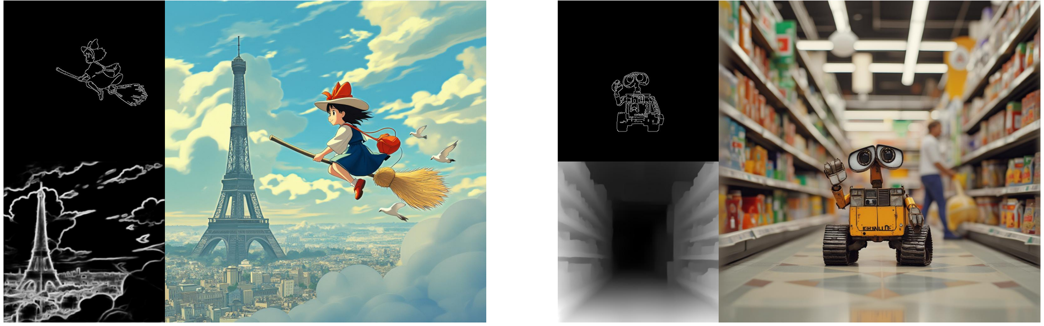

Baby penguin selfie in museum gallery. *Red bicycle, light-purple wall, white window, minimal.*

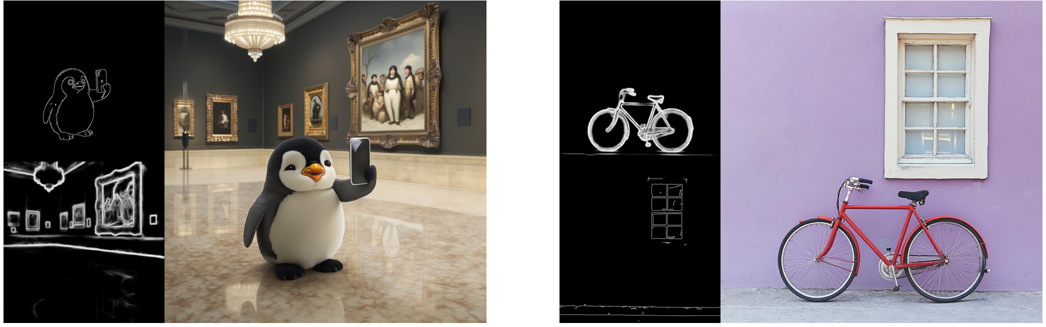

Figure 9: Qualitative results of the Cross-ControlNet on FLUX.1-dev.

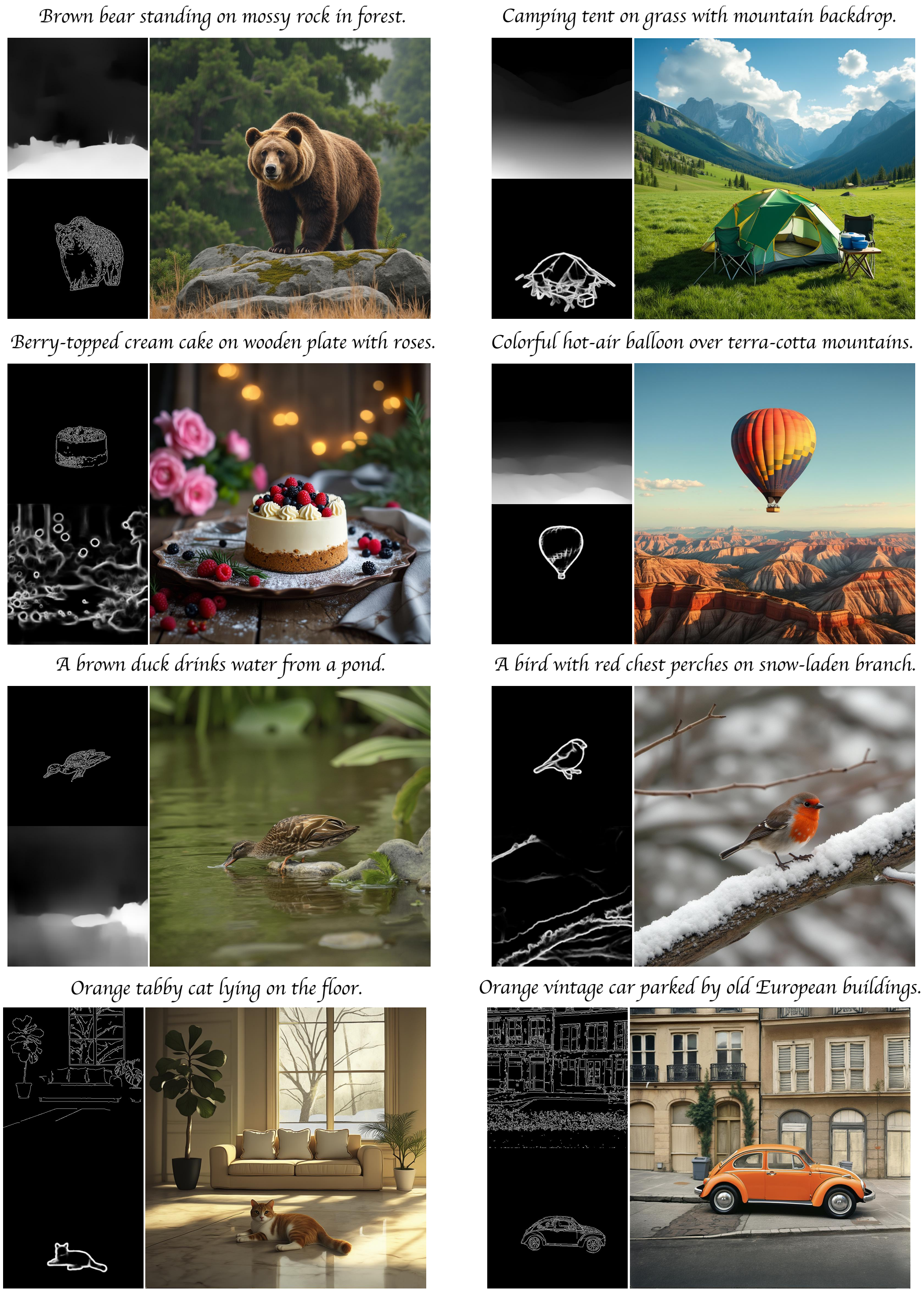

Brown bear standing on mossy rock in forest.

Camping tent on grass with mountain backdrop.

Berry-topped cream cake on wooden plate with roses.

Colorful hot-air balloon over terra-cotta mountains.

A brown duck drinks water from a pond.

A bird with red chest perches on snow-laden branch.

Orange tabby cat lying on the floor.

Orange vintage car parked by old European buildings.

Figure 10: Qualitative results of the Cross-ControlNet on FLUX.1-dev. Because only a limited number of open-source ControlNet extensions are currently available for FLUX, we present conditioning only with Canny, Depth, and HED maps.

An astronaut in a white spacesuit stands on the moon's surface, Earth behind

A cartoon yellow dog and a gray cat, simple line art style, minimal style

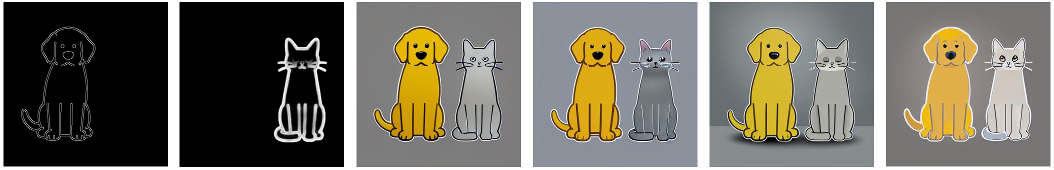

A vintage typewriter on a wooden desk with a bookshelf full of old books in the background, clear typewriter keys

A classic red telephone booth on an empty cobblestone street

A single sailing boat on a calm lake, with snowy mountains far in the background

A single lighthouse standing on a rocky cliff, ocean waves in the background

A vintage camera placed on a wooden desk, blurred bookshelves behind

A cherry blossom tree, with Mt. Fuji faintly visible in the distance, oil painting texture, obvious brushstrokes

Figure 11: More visual results from Cross-ControlNet on Stable Diffusion-v1.5 model.

Cute origami fox in a pastel, whimsical origami forest with polygonal trees—dreamy, playful.

A tall cactus in the desert foreground

Macro, realistic glass terrarium on a wooden desk—lush moss, tiny detailed house, sharp, gentle backlight.

A winter scene with snow - covered ground and a wooden house, frosted trees, and a pale blue sky, quiet and beautiful

Dawn—shepherd with a lantern herds the flock across a rugged, hummocky meadow.

Lion dance in Chinese courtyard, red lanterns, traditional roofs, yellow fluffy lion, blue sky

A hiker on the edge of a canyon, river and rugged cliffs stretching into the horizon, warm morning light,blue sky

Black sunglasses on weathered white marble column, Parthenon on hill under blue sky, soft bokeh, crisp foreground

Figure 12: More visual results from Cross-ControlNet on Stable Diffusion-v1.5 model.

A.7 ALGORITHM

Algorithm 1 PixFusion for Cross-Model Feature Fusion

```
Require: $M_1$ layers $\{l_1^l\}_{l=1}^L$, $M_2$ layers $\{l_2^l\}_{l=1}^L$, conditions $c_1, c_2$, threshold $\delta$, kernels $\mathcal{G}_{\kappa_1}, \mathcal{G}_{\kappa_2}$
for $l = 1$ to $L - 1$ do
    $f_1 \leftarrow l_1^l(c_1); \quad f_2 \leftarrow l_2^l(c_2)$
    $\rho \leftarrow \mathrm{CosSim}\big((f_1 - \mu_1) * \mathcal{G}_{\kappa_2},\ (f_2 - \mu_2) * \mathcal{G}_{\kappa_2}\big)$
    for all position $(j, k)$ do
        if $\rho^{(j,k)} \geq \delta$ then
            $\hat{f}^{(j,k)} \leftarrow \frac{f_1^{(j,k)} + f_2^{(j,k)}}{2}$
        else
            $\hat{f}^{(j,k)} \leftarrow f_{i^\star}^{(j,k)}$, $i^\star = \arg\max_i \big[\mathcal{G}_{\kappa_1} * \hat{\sigma}_i\big]_{(j,k)}$
        end if
    end for
    feed $\hat{f}$ to SD decoder
end for
```

Algorithm 2 ChannelFusion for Cross-Model Feature Fusion

```
Require: $M_1, M_2$ final-layer features $f_1, f_2$, threshold $\delta$
$f_1 \leftarrow l_1^L(f_1); \quad f_2 \leftarrow l_2^L(f_2)$
compute $R_c = 1 - \frac{|\hat{\sigma}_{1,c} - \hat{\sigma}_{2,c}|}{\max(\hat{\sigma}_{1,c}, \hat{\sigma}_{2,c})}$ for each channel $c$
for all channel $c$ do
    if $R_c > \delta$ then
        $w_i \leftarrow \hat{\sigma}_{i,c} \big/ \sum_k \hat{\sigma}_{k,c}$
        $\hat{f}_c \leftarrow w_1 f_{1,c} + w_2 f_{2,c}$
    else
        $\hat{f}_c \leftarrow f_{1,c}$ if $\hat{\sigma}_{1,c} > \hat{\sigma}_{2,c}$ else $f_{2,c}$
    end if
end for
feed $\hat{f}$ to SD decoder
```

Algorithm 3 Cross-ControlNet Inference

```
Require: Foreground model $M_1$, background model $M_2$, masks $M^f, M^b$
Ensure: Denoised latent $z_0$
for $t = T$ to $1$ do
    for $l = 1$ to $L$ do
        $\{Q_1, K_1, V_1\} \leftarrow M_1(t, z_t); \quad \{Q_2, K_2, V_2\} \leftarrow M_2(t, z_t)$
        $Attn^f \leftarrow \text{Attention}(Q_2, K_1, V_1; M^f)$
        $Attn^b \leftarrow \text{Attention}\big(Q_2, [K_2 \oplus K_1], [V_2 \oplus V_1]; [\mathbf{1} \oplus M^b]\big)$
        $\hat{Attn} \leftarrow M^f \cdot Attn^f + M^b \cdot Attn^b$
        if $l == L$ then
            $\hat{f} \leftarrow \text{ChannelFusion}(M_1, M_2; \hat{Attn})$
        else
            $\hat{f} \leftarrow \text{PixFusion}(M_1, M_2; \hat{Attn})$
        end if
        feed $\hat{f}$ to SD decoder
    end for
    $z_{t-1} \leftarrow \text{SD}(t, z_t)$
end for
return $z_0$
```